Automated Electronic Mode Stirring in Reverberant Cavities to Optimize Backscatter Link Margins

Austin Oursland

A thesis
submitted in partial fulfillment of the
requirements for the degree of

Master of Science

University of Washington
2023

Committee:
Matthew S. Reynolds
Joshua R. Smith

Program Authorized to Offer Degree:
Electrical & Computer Engineering

University of Washington

Abstract

Automated Electronic Mode Stirring in Reverberant Cavities to Optimize Backscatter Link Margins

Austin Oursland

Chair of the Supervisory Committee:
Matthew S. Reynolds
Department of Electrical and Computer Engineering

The usage of backscatter communications in metal-rich environments is limited by the deep nulls present due to dense multipath. With the round-trip path losses incurred by backscatter communication links, the system link budget is very sensitive to these nulls. Real-world applications require a strategy to mitigate this path loss actively in a wireless uplink, while conforming to the size, weight, and power constraints of the system. Past research has shown that electronic mode stirring can mitigate the effects of multipath in a static scenario. This work presents an automated reconfiguration strategy that can search through a set of electronic mode stirring states to optimize for improved link margins. The experiments are performed with a 2.4 GHz dual-polarized electronic mode stirring system designed for use within metal animal cages used in neurological research. Path loss measurements represent the spatially dependent multipath, with an animal motion model to simulate a real-time system. Measurements indicate that the system can reduce worst-case one-way path loss by 26 dB in static scenarios. Then, the simulation measures the number of path loss samples which exceed a nominal threshold for reliable communication. The percentage of samples that exceed this path loss threshold in the un-stirred system is 32%, regardless of simulated velocity. Under slow moving conditions, automated reconfiguration improves that percentage of samples exceeding the path loss threshold to 8%, a reduction of 75%. The improvement is less pronounced with fast motion, which results in a percentage of 26%-28% that exceed the path loss threshold. Given a sufficient update rate, this simple reconfiguration strategy could be used to mitigate multipath for backscatter communication.

Acknowledgements

I would like to express my gratitude to my advisor, Professor Matthew Reynolds. His guidance and collaboration throughout my time at UW has been invaluable and allowed me to pursue greater heights in this area of technology. It has been a great experience to work together after taking my first wireless comms. course with you many years ago. I hope to continue our collaboration, even as I move onto the next stage in my research journey.

I also want to extend a great thanks to the other students who have been a part of this journey the last four quarters. Specifically all the students in the lab – Sara Reyes, Kevin Ho, Theodore Moody, Ryan Douglas, Oleg Ianchenko, Madeleine Lee, and Chloe Fong – for the discussions and helping make the lab a fun space to be. And to my colleague from Impinj, Joshua Ensworth. His prior work in this same lab has been a constant source of inspiration. It has been fun to see how far ahead his work was in backscatter systems research. And lastly to James Rosenthal, whose work on the NeuroDisc wireless uplink design served as the foundational component of this project.

I'd also like to thank my wife, Bryn, for helping me manage the negative hours I had in the week to try and fit in school, work, and day-to-day life.

Contents

List of Figures

List of Tables

List of Abbreviations and Symbols

Abbreviations

BCI	Brain-computer interface
BLE	Bluetooth Low Energy
CMOS	Complementary metal–oxide semiconductor
COTS	Commercial off-the-shelf
CW	Carrier wave
LED	Light-emitting diode
MIMO	Multiple-input and multiple-output
MSA	Mode stirring antenna
NHP	Non-human primate
PCB	Printed circuit board
RF	Radio frequency
RSSI	Received signal strength indicator
SPDT	Single pole, dual throw
VNA	Vector network analyzer

Symbols

P_R	The received signal power in a wireless system, at the input of the receiver
P_T	The transmitted signal power in a wireless system, at the input to the transmit antenna
S_R	The minimum signal power needed for reliable signal reception
G_p	The power gain in a wireless system, due to the path
G_p^{-1}	Path loss, as the inverse of the path gain
S_{21}	The forward path voltage gain in a two-port network measurement

Chapter 1

Introduction

This thesis is adapted from the unpublished paper "Automated Optimization of Electronic Mode Stirring for Enhanced Backscatter Link Margin in Reverberant Cavities," to be submitted in December 2023 to the IEEE Journal of Radio Frequency Identification [1]. This thesis also fully describes the integrated dual-polarized electronic mode stirring system developed for the original work by S. M. Reyes, **A. Oursland**, M. Lee, T. J. Moody, and M. S. Reynolds [2].

1.1 Backscatter Communication Systems

Backscatter communication systems offer an extremely power-efficient and low complexity solution for wireless data transfer [3; 4]. These systems transmit data by reflecting an externally-generated carrier wave, eliminating the need for power-intensive frequency synthesis and amplification in wireless devices. These simplifications in backscatter allow for less complex and less power-consuming designs, which can minimize the size, weight, and power requirements of the wireless uplink. However, the round-trip nature of the backscatter link results in reduced link margin, particularly in metal-rich environments having the deep nulls typical of dense multipath. These environments have an uneven distribution of field strength due to constructive and destructive multipath, especially in what is known as a resonant cavity.

A technique known as *mode stirring* allows for the redistribution of the electromagnetic modes which induce the multipath behavior of the environment, thus mitigating the multipath effect for a fixed position [5; 6]. Of specific interest is the electronic mode stirring technique, which leverages a similar principle to the key mechanism of backscatter, that modifies the reflections at specific points in the environment to influence the pattern of multipath in the environment. Electronic mode stirring is also convenient due to the lack of mechanical motion required in the environment, meaning it has wider applicability. This capability to mitigate path loss offers the opportunity to enable backscatter solutions in more applications which are extremely constrained in weight, size, and power.

1.2 Neurological Research Applications

Some relevant emerging applications for backscatter communication are the high bandwidth data uplinks used in biomedical telemetry applications. For example, neuroscience research extensively utilizes neural recordings from non-human primates (NHPs) to explore the relationship between basic neural functions and more complex behavior [7]. Recent progress in the field has resulted in a shift away from tethered (wired) neural recording systems, and toward the use of wireless brain-computer interfaces (BCIs) that hold the promise of providing continuous neural recording from freely-moving animals, with the goal of enhancing the quality of the neural data while minimizing the stress and physical limitations imposed on the NHPs [8; 9; 10].

In the development of wireless BCIs for long-duration neural recording in freely moving animals, one major challenge is the high power consumption of existing wireless data uplinks. The size and weight constraints on BCI batteries, typically limited to $1-3$ cm^3, result in rapid depletion due to the high DC power requirements of standard wireless technologies like WiFi and Bluetooth Low Energy (BLE) [11; 12]. The benefit of reduced power consumption and high energy per bit efficiency have driven the development of backscatter uplink designs [13; 14; 15]. Unfortunately, the non-human primate (NHP) metal-cage environment functions as a resonant cavity. This means that multipath presents a major challenge to these systems. Prior work has indicated that electronic mode stirring could offer mitigation in these NHP environments [16]. This has motivated the design and characterization of such a system to address this issue [2].

Similar work has attempted to leverage multiple-input and multiple-output (MIMO) techniques to mitigate multipath for backscatter systems [17; 18; 19]. However, these solutions have low applicability in the BCI application, as BCIs are usually very small compared to the signal wavelength. Other proposed solutions include designing custom RF-transparent polycarbonate cages [20], which reduce reflections but are both more costly and less durable than metal cages, as plastic materials degrade quickly under frequent autoclave sterilization and chemical cleaning, which is essential in animal care facilities.

1.3 Outline of Content

This thesis presents a system that serves to mitigate multipath losses and improve link margin in reverberant cavities. The system is comprised of an integrated 2.4 GHz dual-polarized electronic mode stirring component and an automated reconfiguration component. It also includes a brief demonstration of the system on an active backscatter uplink within the same metal-cage environment.

1.3.1 Dual-Polarized Electronic Mode Stirring

For the mode stirring system, the original characterization of the 2.4 GHz dual-polarized system is presented. Using four mode stirring antennas, controlled by a single Arduino concentrator, an experiment comprised of 72 positions within a metal-cage environment is presented. This system was able to mitigate the statically measured worst-case multipath, where the greatest benefit is realized by the fully dual-polarized design. The measurements present an improvement in path loss of 14.3 dB, from 59 dB of worst-case one-way path loss to 44.7 dB.

1.3.2 Automated Reconfiguration

The results of this analysis motivated the implementation of an automated reconfiguration system for electronic mode stirring. To characterize the real-time approaches offline, a simulation engine is developed for modeling path loss based on a given position. This includes a model of animal motion for a range of position variations, focusing on a slow and fast moving case. Performance of the system is characterized against a nominal link budget based on the Bluetooth Low Energy specification. The analysis and simulation utilize a set of real measurements from a centimeter-square grid with 2124 positions. The high resolution data presents a measured worst-case path loss well beyond that of the coarse measurement, reaching 75.8 dB in the un-stirred state. The fully-stirred system was capable of reducing this by 26 dB, down to 49.8 dB. As compared to a *well stirred* system, the implemented electronic mode stirring system has a tendency to excite a single dominant mode, presenting a behavior that is to be defined as *sufficiently stirred*. This *sufficiently stirred* criteria accounts for the limited effective control space available to this electronic mode stirring system, since not all possible mode distributions can be reached.

Simulation against a motion model then measures the number of path loss samples which exceed the nominal threshold for reliable communication. The percentage of samples with path loss exceeding this threshold in the un-stirred system is 31%-32%, regardless of simulated motion. Under slow moving, locally stable, conditions, automated reconfiguration improves that percentage of samples with path loss exceeding the threshold to 8%, a reduction of 75%. For fast motion the improvement is less pronounced, for a percentage of 26%-28% that exceed the path loss threshold.

1.3.3 Demonstration

The final section presented is a brief demonstration of mode stirring with a Bluetooth Low Energy backscatter tag. The manual measurement of received signal strength between a backscatter tag and an Android phone provide an early view of what the next step in the development cycle would look like. For the 4 manual measurement positions, the mode stirring contributed the most improvement to the points with the most path loss. These ranges for path loss align with the mean behavior of the high resolution analysis from the prior measurements.

Chapter 2

Dual-Polarized Electronic Mode Stirring

This section is adapted from "Dual-Polarized Electronic Mode Stirring for Improved Backscatter Communication Link Margin in a Reverberant Cavity Animal Cage Environment," [2]. The sections concerning the electrical and mechanical design of the integrated system were the contribution of Sara M. Reyes, Madeleine Lee, and Theodore J. Moody. Contributions by the author relate to the experimental design and analysis.

2.1 Motivation

Common approaches to mitigating multipath interference, such as the use of MIMO links to leverage path diversity, are not practical for the NHP application due to the need to minimize the size, weight, and power of the brain-computer interface (BCI) device. As the size of the BCI device decreases, the effective path diversity decreases, as the antennas on a small BCI device effectively sample the same multipath-heavy channel. Electronic mode stirring in the NHP metal-cage environment has been shown to be effective at modifying the channel to mitigate multipath [16]. The previously developed system utilized to measure this improvement was comprised of discrete components, commercial off-the-shelf (COTS) radio frequency (RF) switch evaluation boards and COTS horizontally-polarized patch antennas that were cabled together to form an electronic mode stirring antenna (MSA). This work presents an integrated solution, comprising of a dual-polarized, air dielectric patch antenna, and a pair of complementary metal–oxide–semiconductor (CMOS) single pole, dual throw (SPDT) RF switches, which is characterized in a reverberant cavity analog of the metal cage.

2.2 Integrated Electronic Mode Stirring System Design

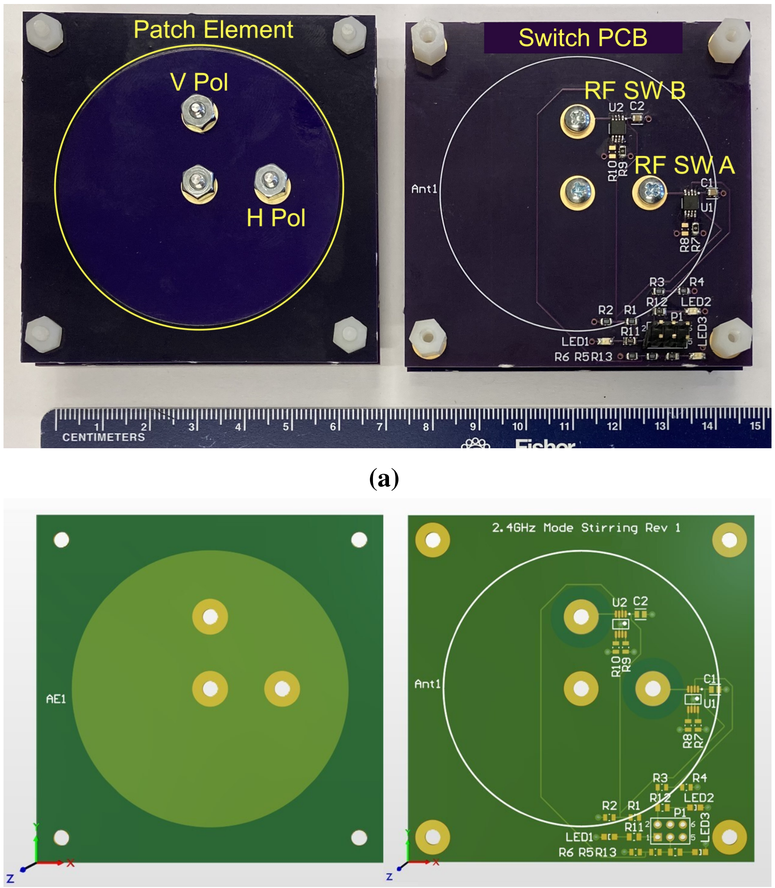

(a)

(b)

Figure 2.1: (a) Photos and (b) printed circuit board (PCB) layouts of the 2.4 GHz mode stirring antenna (MSA) assembly, showing the antenna PCB (left) and the RF switch PCB (right).

The dual-polarized electronic mode stirring system consists of two printed circuit board (PCB) assemblies, the MSA assembly and a concentrator assembly. The MSA assembly integrates all RF functionality, leveraging a 2.4 GHz air dielectric patch antenna and SPDT RF switches attached to a selectable set of loads. The individual PCB for the MSA assembly were fabricated on 0.8 mm, two-layer, FR-4 substrate. The concentrator assembly provides digital control functions. The digital control allows control of multiple MSAs by a PC via a USB connection and a supporting Python driver. The concentrator PCB leverages an Arduino Mega 2560 to provide 5 V logic-level drive signals to an MSA via a 6-pin flat cable. This system is capable of supporting up to eight MSAs at a time.

As shown in Figure 2.1, the layout of the MSA PCB assembly is comprised of a stack of two PCBs. Each PCB contains the same four mechanical mounting points, three electrical connection points for ground, and pair of feed points for the two polarizations of the antenna. The two PCB are separated by 6.35 mm spacers that serve double-duty as mechanical fasteners and electrical feed connections. The two feed points are perpendicular to each other to excite the vertical and horizontal polarization modes. Based on simulation results from CST Microwave Studio, the feed points are spaced approximately 14 mm from the center to yield a 50 Ω feed point impedance.

The top PCB contains the 28 mm radius, dual-polarized, circular, patch antenna. The bottom PCB contains a ground plane on the upper layer with two CMOS SPDT RF switches (Analog Devices ADG919). Both switches are placed as close as possible to their respective feed points to minimize microstrip losses. Each switch is configured to present either a short circuit or open circuit, which results in a 180-degree phase shift for reflected signals in that polarization.

Voltage dividers are included to convert the 5 V logic-level signal to 2.5 V – below the maximum voltage rating of 2.75 V for the RF switches. Diagnostic light-emitting diodes (LEDs) are also included to indicate the RF switch state. Figure 2.2 displays the full block diagram of the control logic from the concentrator to the MSAs, including the logic and terminations at the SPDT RF switches.

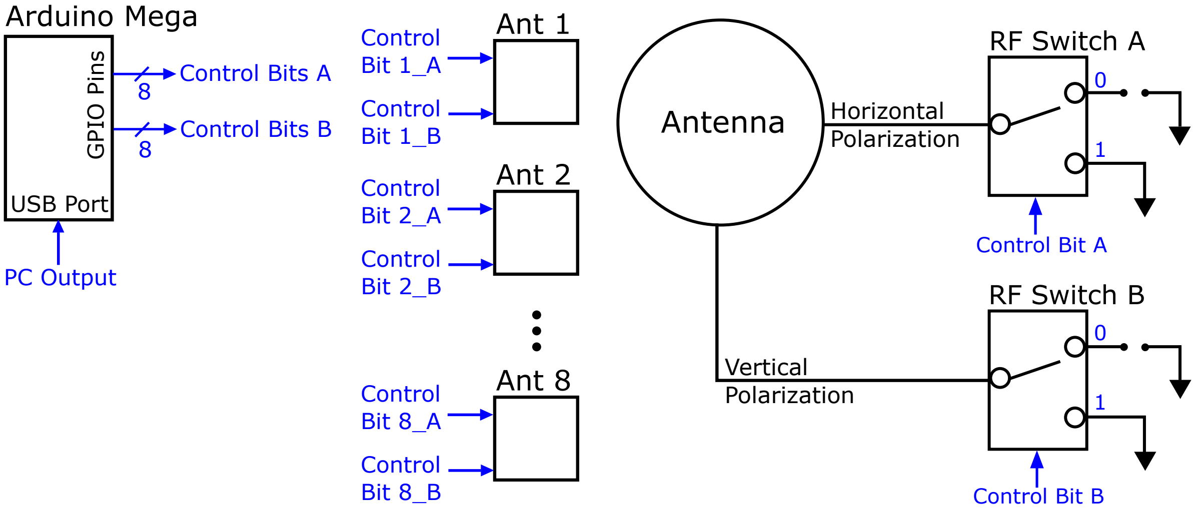

(a) (b)

Figure 2.2: (a) Block diagram of the concentrator control logic signals and (b) the mode stirring antenna (MSA) with RF switch states (open and short).

2.3 Experimental Setup and Results

A commercial off-the-shelf (COTS) pet crate is used to represent the bulky, floor-mounted metal cage environment. This allows the cage analog to be easily placed on a bench top for measurement and repositioning of the BCI. The crate is wrapped in a bronze mesh, of 1 mm spacing, to increase the number of resonant modes within the cavity at the 2.4 GHz industrial, scientific, and medical radio (ISM) band. By reducing the amount of signal leakage through the relatively large gaps in the crate, the mesh-wrapped pet crate functions as a resonant cavity. Four MSAs were mounted within the cage and placed to cover distinct quadrants. The concentrator assembly was then mounted to the top of the cage and wired to the MSAs through additional holes in the mesh wrapping. A photo of the cage with mounted equipment is shown in Figure 2.3a.

An experimental campaign was undertaken using one linear-polarized cage-mounted antenna (L-Comm Inc. HG2048P) and the BCI antenna (2.4 GHz monopole antenna). The BCI was mounted atop a tissue proxy, comprised of 0.5 L of 0.91% saline solution to simulate the body of the non-human primate. Twenty four measurement positions on a 10.1 cm x 10.1 cm grid were chosen over three planes (5 cm Z-axis spacing), starting from the floor of the cage plus the height of the tissue proxy. A Keysight vector network analyzer (VNA) is used to measure the forward voltage gain (S_{21}) of the system, between the cage-mounted antenna and the BCI, over the 2.4 GHz ISM band (2400-2483 MHz, at steps of 500 kHz). This measurement was then repeated for all combinations of RF switch state for the electronic mode stirring system (256 total states for 4 MSAs). A block diagram of the full setup is recorded in Figure 2.3b.

For the analysis of a wireless uplink, the inverse magnitude of S_{21} is converted to a one-way path loss, as described in equation 2.1.

$$\begin{aligned} G_p &= |S_{21}| \\ 20\log_{10}\left(G_p^{-1}\right) &= \text{One-way path loss dB} \end{aligned} \tag{2.1}$$

By measuring the path loss of the system at each mode stirring state, the worst-case and best-case path loss can be determined for all positions. The data was organized and analyzed based on which polarization was preferentially scattered by the MSAs. The case without mode stirring (baseline) involved removing power from the concentrator board, which has the effect of terminating the mounted MSAs to a near-50 Ω load (1 state). The vertical polarization data is comprised of all mode stirring states that had horizontal RF switches

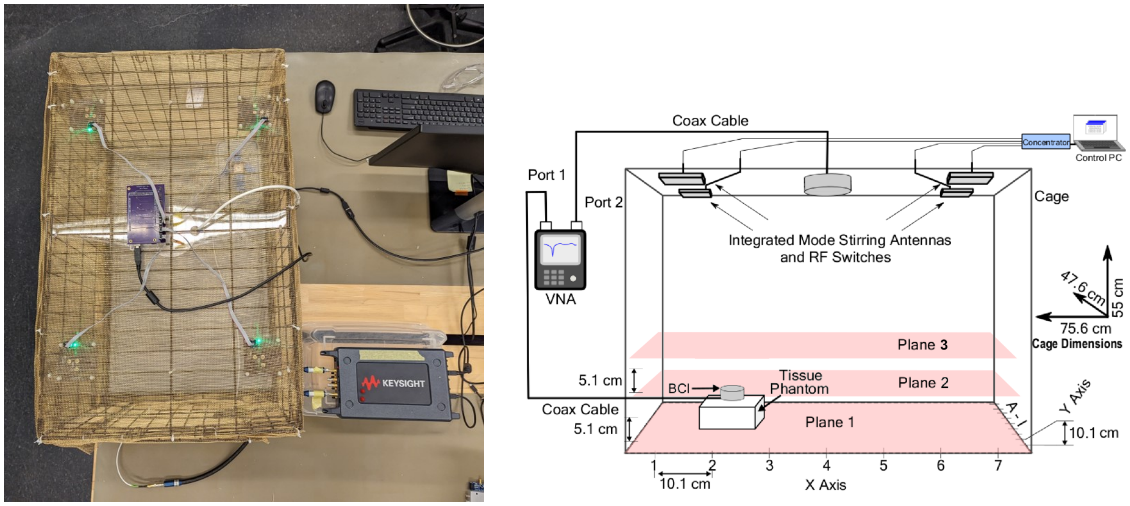

(a) **(b)**

Figure 2.3: (a) Photo and (b) block diagram of the test setup used to characterize the 2.4 GHz ISM-band wireless channel inside the test cage.

left in the open-circuit terminations, allowing only vertical switches to vary (16 states). The horizontal polarization data was analyzed analogously. Finally, the dual-polarization data is comprised of all possible mode stirring states (256 states).

For each of the data sets, the S_{21} measurements are converted to one-way path loss and used to compute a state-specific worst-case for that position. The worst-case is the maximum one-way path loss over the frequency range, such that the least power reaches the BCI. For the single and dual-polarization data, the mean and standard deviation of the possible worst-case over mode stirring state is recorded for each position. Then for the set of possible mode stirring states available, the optimal stirring result is assigned to that position. The optimal one-way path loss is the minimum over possible mode stirring states. This leaves a single measurement at each position over the three planes for each electronic mode stirring scenario.

2.3.1 Results

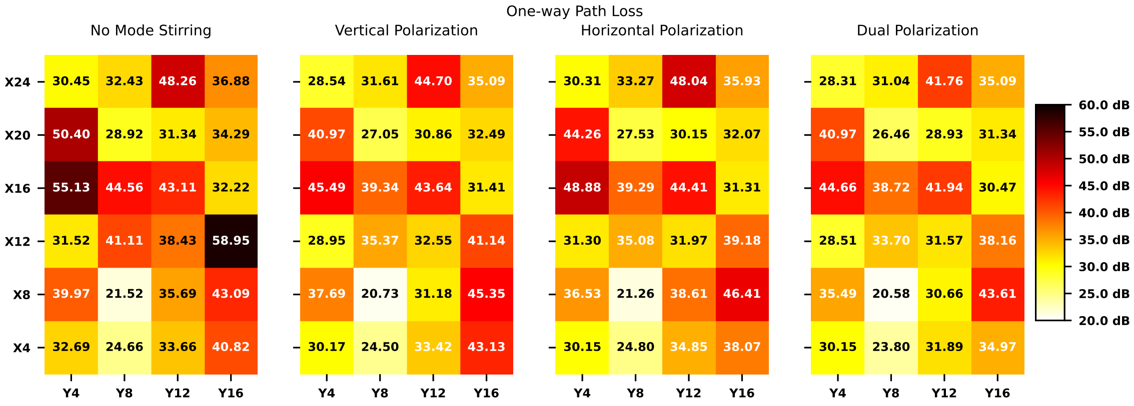

(a) Plane 3: Z = 0 cm (Cage floor)

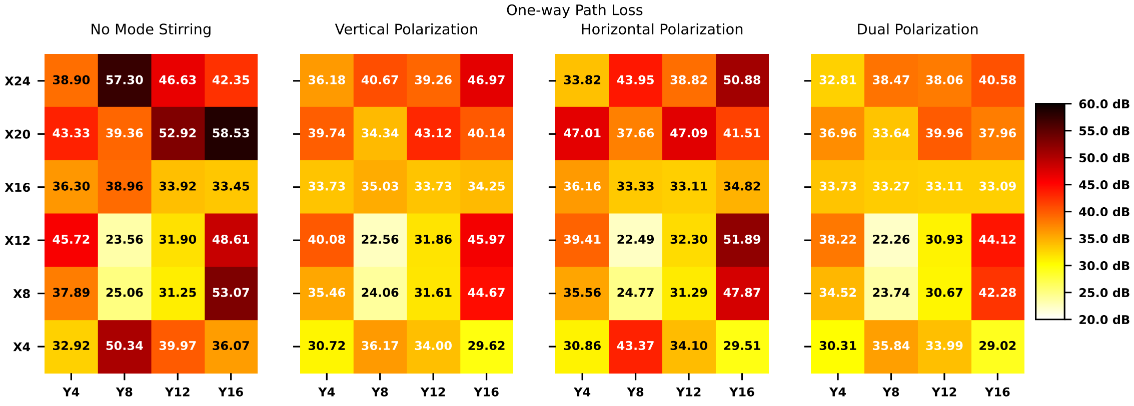

(b) Plane 3: Z = 5 cm

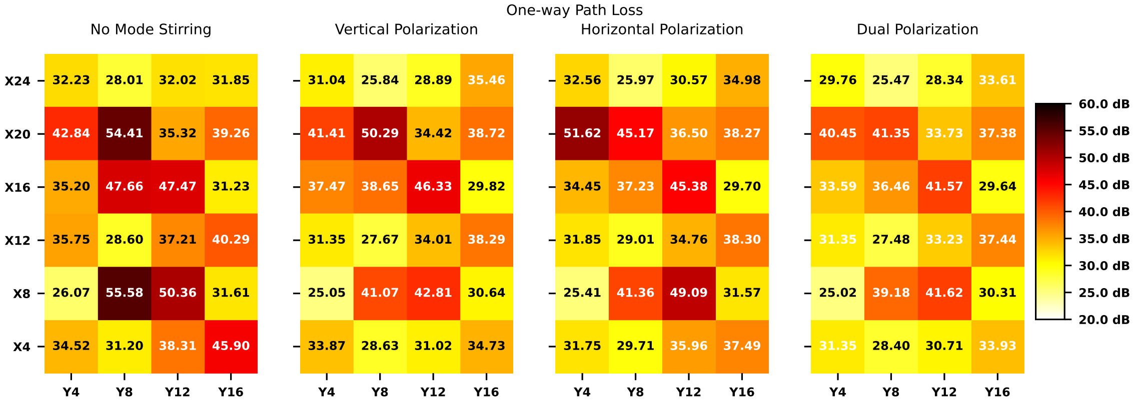

(c) Plane 3: Z = 10 cm

Figure 2.4: (a,b,c) Heat map showing measured one-way path loss at each of the 72 surveyed locations in the test cage, where lighter colors indicate better performance.

Table 2.1: 2.4 GHz One-way Path Loss Measurement Summary Over All Planes (Decibels)

	Without MS	With MS Vertical pol.	With MS Horizontal pol.	With MS Dual pol.	Dual pol MS vs. without MS
Worst-Case	59.0	50.3	51.9	44.7	-14.3
Mean	26.1	25.9	26.0	25.8	-0.3
σ	4.3	3.8	4.0	3.6	-0.7

Table 2.2: 2.4 GHz One-Way Path Loss Measurement Summary Comparing Dual Pol. Only (Decibels)

	Plane 1			Plane 2			Plane 3		
	Without MS	**Dual pol. MS**	**Change**	**Without MS**	**Dual pol. MS**	**Change**	**Without MS**	**Dual pol. MS**	**Change**
Worst-Case	59.0	44.7	14.3	58.5	44.1	14.4	55.6	41.6	14.0
Mean	25.6	25.3	0.3	26.6	26.2	0.4	26.2	25.8	0.4
σ	4.1	3.6	0.5	4.6	3.8	0.8	4.2	3.5	0.7

Figure 2.4 presents the series of heat maps from the analysis, showing the measured worst-case at each of the 72 surveyed positions. These heat maps show the one-way path loss at each location with no stirring, vertical polarization only, horizontal polarization only, and with dual-polarization.

Table 2.1 and Table 2.2 summarize the top-level statistics of the observed results. The use of dual-polarized electronic mode stirring is shown to improve the worst-case one-way path loss across all surveyed locations by 14.3 dB. The mean one-way path loss was also improved by 0.3 dB given this cage setup.

The reported improvement from [16] was recorded in two-way insertion loss and was noted as a 35.6 dB improvement in the actual NHP environment. Two-way insertion loss is a synonym for the two-way path loss. This implies that the reported improvement from the prior work was 17.8 dB in one-way path loss. This deviation in the results shown in Figure 2.4 and Table 2.2 as compared to the prior work is likely due to the much more extreme worst-case measured in the actual NHP environment. The worst-case in this bench measurement was 59.0 dB, while the worst-case in the prior work was over 74 dB of one-way path loss.

2.4 Conclusions

This chapter presented a novel dual-polarized electronic mode stirring system operating for usage in the 2.4 GHz ISM band. The initial testing of performance, in an facsimile of the NHP metal cage environment, improved a baseline 59 dB worst-case one-way path loss to 44.7 dB with the usage of electronic mode stirring. The improvement of 14.3 dB in worst-case one-way path loss represents the ability of the system to improve the link margin of a backscatter system operating within a reverberant cavity. This same measurement also indicated a distinct benefit to the individual control of the two polarization states of the antenna.

Chapter 3

Automated Reconfiguration

This section is adapted from the authors contributions in the unpublished paper "Automated Optimization of Electronic Mode Stirring for Enhanced Backscatter Link Margin in Reverberant Cavities," to be submitted in December 2023 to the IEEE Journal of Radio Frequency Identification [1]. The portions relating to the development of the simulation framework are the contribution of Oleg Ianchenko and the author. Ryan Douglas contributed the development of the two-axis motion controller.

In this work, the integrated electronic mode stirring system described in the previous chapter, [2], is leveraged to develop an automated solution to mitigate multipath. An improved measurement of the reverberant cavity allows the development of a system model with animal motion. By using the animal motion model, the ability of the electronic mode stirring system to dynamically improve the worst-case one-way path loss is characterized. It also, for the first time, analyses the *well stirred* criteria of the system.

3.1 Motivation

Thanks to the shift away from tethered (wired) neural recording systems, in favor of wireless brain-computer interfaces (BCIs), the stress and physical limitations imposed on the non-human primates (NHPs) is reduced [8; 9; 10]. This freedom of motion also means that the wireless uplink will experience a dynamic channel that results in a variable multipath response. The wireless uplink will need to overcome this dynamic multipath to maintain reliable communication. With backscatter uplinks, this effect is more extreme as the link experiences the multipath impairment in the forward and reverse channel. As previously shown, electronic mode stirring is capable of mitigating static multipath impairment in reverberant cavities [16; 2]. To implement electronic mode stirring system in dynamic applications, real-time reconfiguration strategies must be explored. The goal of an automated reconfiguration system should be to reduce the path loss between the transceiver and the BCI. This work proposes a simple, real-time technique to reduce the impact of multipath in the BCI application.

3.2 Strategy

To characterize real-time reconfiguration strategies, a very accurate spatial model of path loss in the cage is required. This model can be comprised of measured data from the reverberant chamber at a very fine resolution. By sampling a very dense grid of points, well below the wavelength of interest, a robust representation of the multipath nulls will be captured. For the modeling in this work, a centimeter-square grid is of interest because we are operating in the 2.4 GHz ISM band with a wavelength around 12.5 cm, so the grid sampled finer than $\lambda/10$. This improved-resolution data is then fed into a simulation engine designed to represent a real time system. The simulation engine must also implement an animal motion model that drives the selected position for each sample. A complete simulation engine flow is recorded in Figure 3.1.

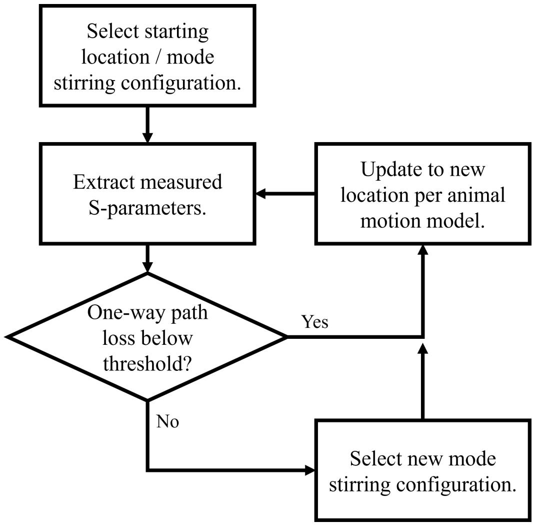

Figure 3.1: Flow chart for real-time system model in simulation, it requires spatially accurate path loss model of cage and animal motion model. Reconfiguration strategies will each be simulated using this technique – *Baseline* (no mode stirring), *One-bit*, and *Random*

In this simulation engine, each measurement is compared against a path loss threshold that is based on a nominal link budget. In the case of a mono-static backscatter system, the following terms can describe a simplified link budget for reliable reception (equation 3.1): receiver sensitivity (S_R), received power (P_R), transmitted power (P_T), transceiver antenna gain (G_A), backscatter loss (G_B^{-1}), and one-way path loss (G_P^{-1}). The link budget dictates that the received signal power must be greater than or equal to the sensitivity of the receiver for reliable communication. The mono-static received power can be approximated as the transmit power being scaled by the antenna gain twice, the one-way path loss twice, and the backscatter loss once. An upper-bound on one-way path loss can be derived using this link budget (equation 3.2).

$$S_R \leq P_R \approx \frac{P_T G_A G_A}{G_B^{-1} G_P^{-1} G_P^{-1}} = P_T G_A^2 G_B G_P^2 \tag{3.1}$$

$$\begin{aligned} G_P^2 &\approx \frac{P_R}{P_T G_B G_A^2} \\ \implies G_P^{-1} &\approx \sqrt{\frac{P_T G_B G_A^2}{P_R}} \\ \therefore G_P^{-1} &\lesssim \sqrt{\frac{P_T G_B G_A^2}{S_R}} \end{aligned} \tag{3.2}$$

For this analysis, backscatter loss and antenna gains will be lumped to together to simplify as a margin term (M). This leaves the receiver sensitivity, transmit power, and margin terms to define a bound for one-way path loss.

$$G_P^{-1} \lesssim \sqrt{\frac{P_T}{P_R} M} \tag{3.3}$$

As prior work utilized a Bluetooth Low Energy (BLE) compatible uplink for the BCI, we will compare to the BLE specification [21; 22]. The Bluetooth 5.3 specification indicates that a Class 1.5 Bluetooth Low Energy (BLE) transmitter has a maximum power output power of 10 dBm. It also specifies that the unencoded receiver sensitivity must be less than or equal to -70 dBm for the 1 Mbps data rate. To accommodate receivers with improved sensitivity, antenna gains, and unknown backscatter losses, a margin term of 10 dB will be applied. Converting to decibels, this results in a maximum allowed one-way path loss of 45 dB (equation 3.4).

$$20 \log_{10} G_P^{-1} \lesssim \frac{10 + 70 + 10}{2} = \frac{90}{2} = 45 \text{ dB} \tag{3.4}$$

3.3 Automated Optimization

For the simplest real-time system, there is no assumption that the position of the BCI is known for any given measurement. Therefore, the system must be able to independently adapt to changes in path loss caused by BCI motion. The simulation utilizes the measured forward voltage gain (S_{21}), which can be used to infer one-way path loss. If the system detects an excessive path loss, then it can leverage electronic mode stirring to mitigate the current multipath state. To do so dynamically, the system will need some strategy for choosing what the new mode stirring state should be. The strategies that are compared in this work are:

- *Baseline:* This is the system at a random, fixed, state. This randomizes the initial distribution of nulls in the environment, but it cannot leverage other electronic mode stirring states to mitigate them.
- *One-Bit Search:* If the path loss exceeds the threshold, the system will flip a random bit in its configuration, changing the state of just one antenna in one polarity. This is the set of configurations with a Hamming distance of 1 from the current state.
- *Random Search:* If the path loss exceeds the threshold, the system will randomly select a new configuration from all possible options.

In all cases, an underlying animal motion model is used to represent the motion of the BCI during operation. This animal motion model is based upon Brownian motion, which is implemented as a multivariate Gaussian process on the change in position of the BCI after each sample. The process will have zero mean and a covariance matrix comprised of $\sigma_{dist}^2 I_2$. This σ_{dist} term describes the standard deviation of motion per update in any direction during the simulation. The mean magnitude of this multivariate process has a well described quantity, based on the Rayleigh distribution ($\mathbf{R}(\sigma_{dist})$), shown in equation 3.5.

$$\mu\left(\mathbf{R}(\sigma_{dist})\right) = \sigma_{dist}\sqrt{\frac{\pi}{2}} \tag{3.5}$$

This ultimately describes the relationship between the real-time system update rate and the mean animal motion or BCI velocity. Letting f represent the frequency of samples/updates in Hz, and s the average velocity of the animal, we can derive equation 3.6.

$$s = f\sigma_{dist}\sqrt{\frac{\pi}{2}} \tag{3.6}$$

If the system is to be run at 200 Hz then a deviation of 0.1 cm would be equivalent to a mean animal motion velocity of 25.1 cm/s. Notably, scaling the system update rate allows for this same level of deviation to represent a proportionally scaled velocity. In a system with known animal motion velocity, the equivalent deviation rate could be computed for any given update rate.

This motion deviation term represents how likely the path is to change at each update step in the simulation. If the change in position is small relative to the wavelength being considered then the path is likely very similar. In this case the simulated grid will be at the centimeter-square level, well below the wavelength of 12.5 cm. How stable this path is between samples defines a classification for the type of motion being observed. For this analysis, the chosen classifications are: quasi-static (50 samples per update), slow moving (10 samples per update), and fast moving (1 sample per update). Since fast motion guarantees every path will be a new path, further classification would require an analysis of how far it could move it a single update.

If we simulate Brownian motion across a set of possible σ_{dist} and look for the distribution of samples it takes to reach 0.5 cm offset in x or y offset, we can classify a set of deviations into those groups. Shown in Figure 3.2, the resulting empirical probability density function (PDF) is shown for a range of deviations from 0.1 cm to 0.9 cm. These motion simulations contained one-hundred thousand trials, each running until either the offset was exceeded or 50 updates, the limit for the quasi-static case.

An example of slow moving case is the 0.1 cm deviation per update, with a median of 14 static samples. The 0.3 cm deviation case is somewhere between a slow and fast moving scenario, with a median of 3 static samples. For the larger deviations, they describe varying degrees of motion that encompass larger and larger areas of space that can be covered per sample, though to a single position they all constitute a fast moving target with a median of 1 static samples. In the analysis of the techniques, this set of deviations will be used to determine how effective electronic mode stirring is under motion.

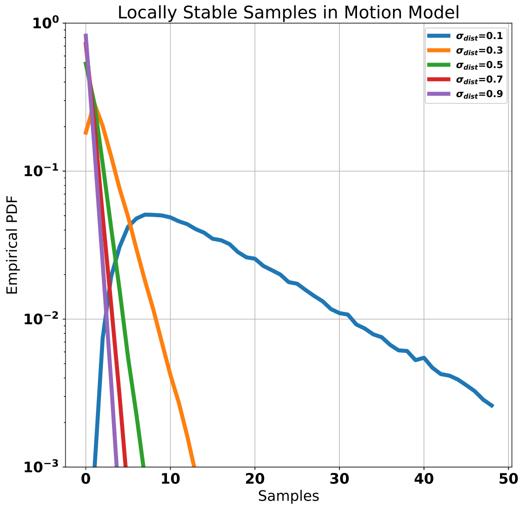

Figure 3.2: Empirically derived probability density function for the local stability of the multipath effect on the BCI under the animal motion model, simulation capped at 50 position updates. Shown in log scale for the y-axis.

3.4 Two-Axis Motion Controller

To measure the cage environment accurately enough for this analysis, an improved BCI positioning technique is implemented. In prior works [16] [2], the BCI was manually moved between measurements to a limited set of positions within the resonant cavity environment. This manual movement made it difficult to repeat measurements at a given position reliably and limited the types of measurement scenarios that were possible. In this work, a three-axis Newport ESP301 motion controller is integrated into the test fixture, with a fixed third axis. The motion controller enables a fine spatial resolution, with accuracy in movement down to 1 mm, and full automation of the test system.

Two 600mm motion stages (Newport IMS600BPP), alongside a wooden dowel and a 3-D printed mounting disc, are put together to form a simple plane of motion for positioning the BCI antenna. The dowel is mounted to the motion stages using a pair of structures, which apply a tension-force to reduce BCI vibration and maintain a 7 cm height above the floor of the cage during motion. The ESP301 is controlled via a Python serial interface that allows for fine-tuned control of the position, velocity, and acceleration of each axis. A calibration set of three positions is referenced to ensure the accuracy of the positioning at the start of each test, with the zero-position located 5 cm from the corner of the crate in both the x and y axis.

3.5 Measurement Fixture

The metal cage assembly, with MSAs and concentrator attached as shown in Fig. 3.3, is then setup next to the two-axis motion controller. In the front of the crate, a gap in the bronze mesh allows for the dowel to freely move within the crate. The total movement range of the BCI exceeds that of the space within the crate available, so the sweep is constrained to a centimeter-square grid over a 58x35 cm area (2124 positions).

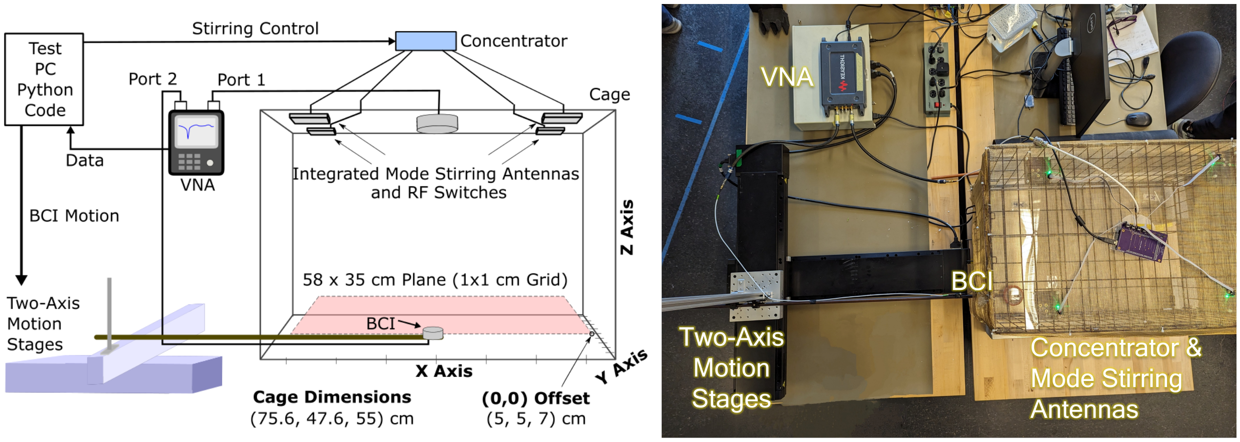

(a) **(b)**

Figure 3.3: (a) The block diagram of the automated test setup with (b) an overhead view of the physical system.

A Keysight vector network analyzer (VNA) is then attached to the cage-mounted transmit antenna and the BCI (2.4 GHz monopole, and L-Comm Inc. HG2048P). In the automated test code, the VNA is used to measure the scattering parameters, including S_{21}, remotely. As the motion controller steps through the coordinate grid, the concentrator iterates through all of the electronic mode stirring states and triggers VNA measurements of two-port network behavior over the 2.4-2.483 GHz band, which uses 500 kHz steps (167 frequency points). The measured VNA data is recorded in complex format to allow for magnitude and phase analysis.

3.6 Analysis Techniques

For the centimeter-square grid data, the system performance is analyzed in terms of worst-case one-way path loss and mode stirring behavior. The first method analyzes the amount of improvement in the worst-case path loss under a variable number of mode stirring antennas. The second method characterizes how well stirred the system is over frequency and across all positions.

This path loss analysis follows from the prior chapter – section 2.3, equation 2.1, involving the conversion of S_{21} into one-way path loss. For each position and state, the worst-case over frequency is found as the maximum one-way path loss. In contrast to the previous analysis, individual sets of the data are arranged from the data based on the number of desired MSAs. The number of states per set is based on the number of active MSAs. A reference configuration, with all RF switches in the open state, is selected as the comparison point for these sets. Then, the minimum worst-case pass loss in each set is assigned to each position. What remains is a heat map of worst-case path loss over all positions in the crate for each set of mode stirring states. The statistics from this heat map can be compared to the reference configuration as an indicator of improvement per antenna.

To analyze the mode stirring behavior of the system, the *well stirred* criteria will be evaluated. Mode stirring effectiveness is typically discussed in terms of reaching statistical field uniformity in an environment [23; 24]. That is to say, we can treat any single point in the environment as similar to any other over the state space even though they are very different for a specific stirring state.

A result of statistical field uniformity is that many modes will be excited over the range of the stirring space at a given position [24]. If the un-stirred component of the electric field is removed from the measurement, then the over-moded ensemble of stirring states will cause any remaining rectangular electric field component to converge to a zero-mean, circularly-symmetric, bivariate normal distribution. This implies that the magnitude of the stirred field strength component will be Rayleigh distributed.

In the case of this automated system, the goal is not necessarily to reach statistical field uniformity. Instead, the automated system attempts to improve link margin by removing only the worst components of the multipath. In these scenarios, it can often be the case that the contribution of a single antenna can be the difference between reliable communication and a dense null. Under this modified criteria, there can arise a strong non-central component in the distribution. A Rician distribution describes the magnitude of this type of distribution, which is circularly symmetric around some offset vector. The Rayleigh distribution happens to be a special case of this scenario, where the offset vector is zero. It is therefore of interest to evaluate this system over both criteria, and we therefore consider the Rician to be a *sufficiently stirred* result.

Unlike the path loss analysis, the forward voltage gain (S_{21}) data is left in complex form initially. To remove any un-stirred component from the data set, the mean value over stirring states ($\langle S_{21} \rangle$) will be removed at each position and frequency (equation 3.7).

$$S_{21,stirred,i} = S_{21,i} - S_{21,unstirred,i} \approx S_{21,i} - \langle S_{21} \rangle \tag{3.7}$$

From this new set of complex vectors, the stirred magnitude for all stirring states can be computed for distribution analysis. The distributions will be compared using a goodness-of-fit test, to determine the likelihood that the data matches the expected model. The Anderson-Darling statistic is computed against an empirical distribution function for each sample set. This statistic is used in an upper-tail test for a the null-hypothesized target distribution (H_0), such that statistic values above some critical value reject the null hypothesis. The critical value is based the desired α of the upper-tail test, or Type I error. This distribution test is performed against both the *well* and *sufficiently stirred* criteria, for all positions and frequencies. The critical value used in this instance is equivalent to $\alpha = 0.05$, which has been prescribed to be 1.341 [23]. Finally, over all positions, the percentage of positions that meet the criteria at a given frequency will be recorded. This percentage metric will indicate how *stirred* the system is across the ISM band within the cage.

3.7 Experimental Results

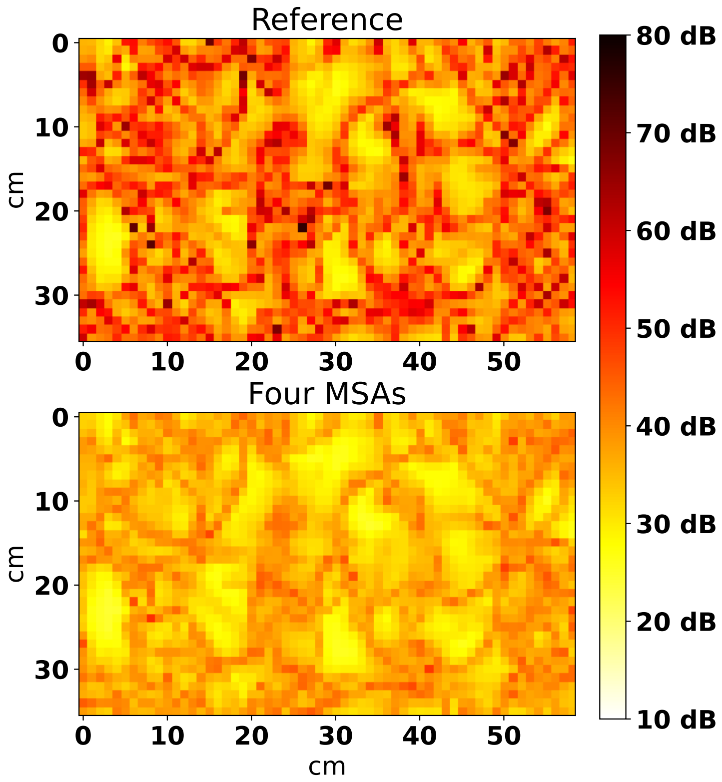

Figure 3.4: Heat map of the worst-case one-way path loss magnitude for the reference and fully stirred cage over the centimeter-square grid (59x36 positions). Lighter colors indicate better performance.

Table 3.1: Optimally-Stirred Worst Case Path Loss (Decibels)

	ISM Band (2.4-2.483 GHz)				
# of MSAs	**Max**	**Δ_{Max}**	**Mean**	**σ**	**Above 45 dB**
Reference	75.8	N/A	41.8	8.5	32.0%
One	63.3	**12.5**	39.4	6.6	20.4%
Two	58.4	**17.5**	37.6	5.5	10.3%
Three	54.3	**21.5**	36.3	4.8	3.6%
Four	49.8	**26.0**	35.2	4.4	0.9 %

The reference scan indicated that there were 32% of positions that exceed the link budget threshold without electronic mode stirring. This can be observed in Figure 3.4, which displays the worst-case one-way path loss over all positions for the reference and fully-stirred cage. This included a worst-case one-way path loss of 75.8 dB in the reference, which exceeded that of the previous coarse grid measurement and the original measurement performed in the NHP metal cage [2; 16]. The most extreme nulls measured in this environment are typically surrounded by other challenging path scenarios, indicating local similarity in the destructive interference. A statistical analysis for these results over the number of active mode stirring antennas (MSAs) is shown in Table 3.1.

The baseline improvement from dual-polarized electronic mode stirring in this fine-resolution scan indicated that even just a single antenna resulted in the worst-case being improved by 12.5 dB, with an additional 4-5 dB of improvement per additional MSA. This also dramatically reduced the standard deviation in the path loss from 8.5 dB to as low as 4.4 dB in the four MSA system. Notably, as the number of antennas increased, the number of points that exceed the threshold of 45 dB are reduced to less than 1%.

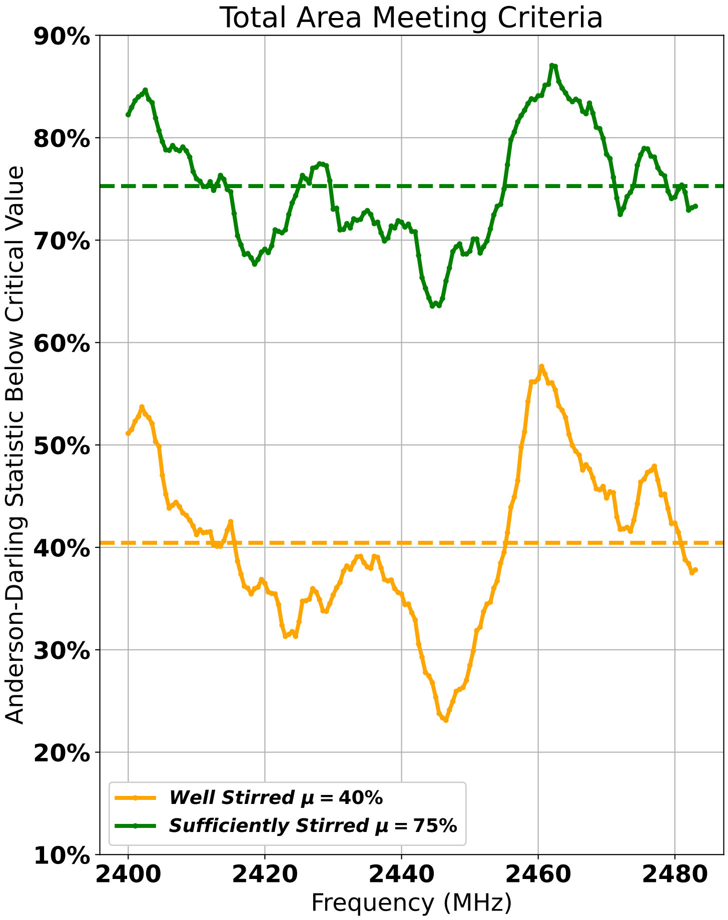

Figure 3.5: Percentage of positions that satisfy the well (Rayleigh) and sufficiently (Rician) stirred criteria over frequency.

Figure 3.5 displays the percentage of positions in the environment which do not exceed the critical value for the *well* and *sufficiently stirred* criteria. Every frequency in the band is *sufficiently stirred* in at least 60% of positions, as compared to the *well stirred* case which is never reaches 60% of positions for any frequency. This is also observed as a gap of 30-45% of positions between the two criteria, which aligns with the mean value across frequency of 75% of positions being *sufficiently stirred* and 40% being *well stirred*. The median criteria was also found at each frequency, to approximate a typical statistic for each frequency. The mean of this typical value across frequency was found to be 1.801 in *well stirred* scenarios and 0.699 for *sufficiently stirred*.

3.8 Optimization Results

With the combination of this high resolution model for the cage environment and the animal motion model previously described, the real-time system simulation can be performed. The simulation of the three reconfiguration strategies was undertaken over a variety of motion scenarios and MSA configuration states. Running a thousand trials, each with a thousand samples, of each strategy over various motion models allows a representative sampling of all positions in the cage ($\sigma_{dist} \in \{0, 0.1, 0.3, 0.5, 0.7, 0.9\}$). The data is presented as a percentage of samples that exceed the one-way path loss threshold. The analysis focuses on the localized motion case (slow moving), the performance while varying animal velocity, and the effect of limiting the number of MSAs in the system.

3.8.1 Localized Motion

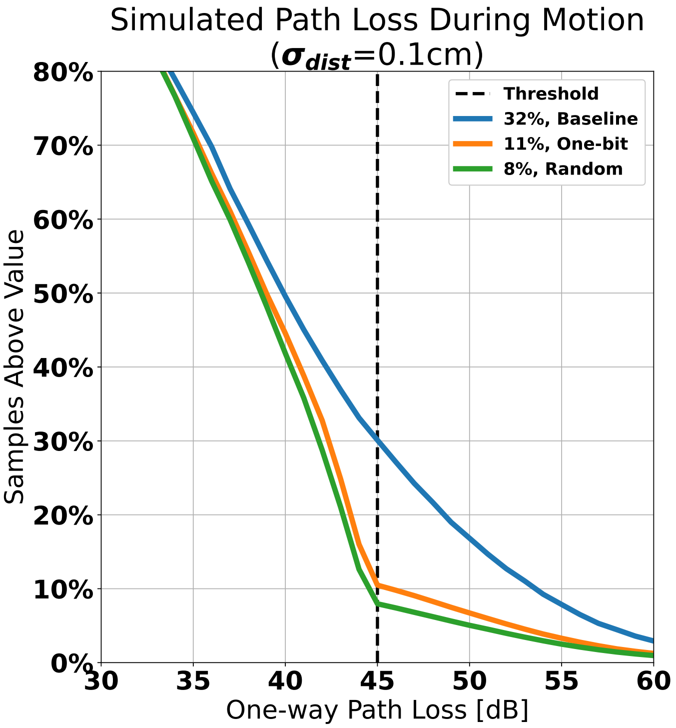

Figure 3.6: Comparison of samples that exceed the threshold for the *Baseline*, *One-bit*, and *Random* reconfiguration strategies, each simulated with Brownian motion with a σ_{dist} of 0.1 cm per sample.

Based on the classifications of the motion model, the σ_{dist} =0.1 cm (slow moving) case serves as the key data point for localized motion performance. For the million samples recorded in each simulation, a plot of the percentage of samples exceeding any given path loss is presented in Figure 3.6. This figure includes a line indicating the path loss threshold and records the percentage of samples that exceeded it. In the baseline case, without mode stirring, 32% of samples exceeded the path loss threshold. The one-bit and random strategies both resulted in an improvement, reducing the numbers of samples exceeding the path loss threshold to 11% and 8% respectively. Between the two techniques, random presented the greatest improvement for local-motion, a reduction of approximately 75% of samples.

3.8.2 Varying Animal Velocity

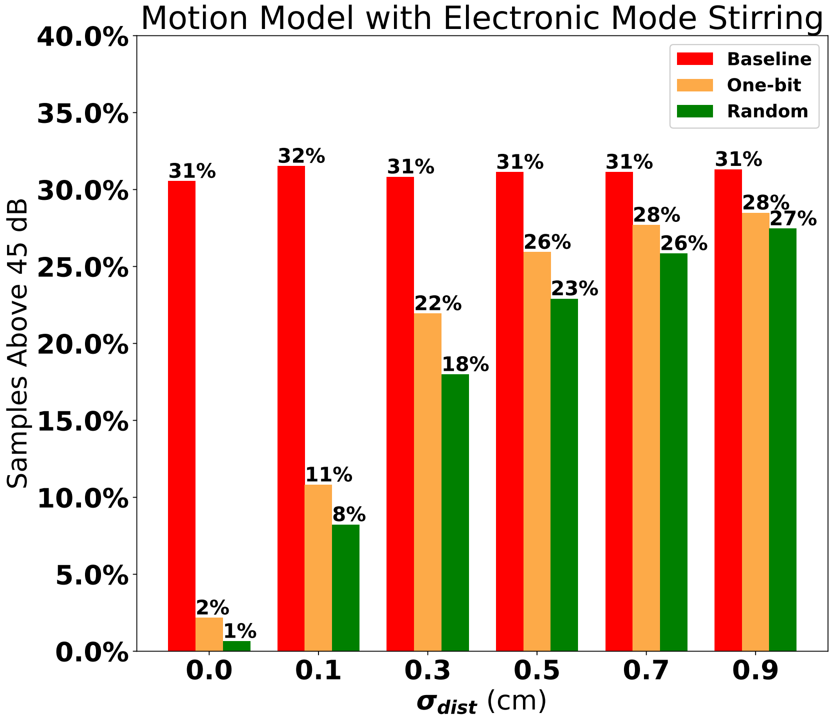

Figure 3.7: Comparison of samples that exceed the threshold for *Baseline*, *One-bit*, and *Random* reconfiguration strategies, presented over a range of σ_{dist} for the Brownian motion model.

Fig. 3.7 summarizes the percentage of samples exceeding the one-way path loss threshold for the strategies as σ_{dist} was increased. Without mode stirring, the percentage is always between 31% and 32%, which aligns with the analysis from the static heat map data. In the static motion case, the one-bit technique was only able to reduce the percentage of samples exceeding the threshold to 2% due to the limited search space, and likely longer convergence times. In the random reconfiguration case, the percentage was reduced to 1%, which aligns with the static data, meaning that random was capable of converging quickly in the 1000 samples of the simulation. This behavior is observed across all deviations, showing that the random strategy has a slight edge over the one-bit search strategy. Utilizing the one-bit or random reconfiguration techniques offers an improvement across all deviation rates, though the improvement degrades as motion reaches the fast motion case, where motion is stirring the path at every sample. When σ_{dist} reaches 0,7 cm (fast motion), the difference between the various strategies is greatly reduced, resulting in approximately 28% of samples exceeding the threshold for the one-bit case and 26% for the random case.

3.8.3 Random Antenna Combinations

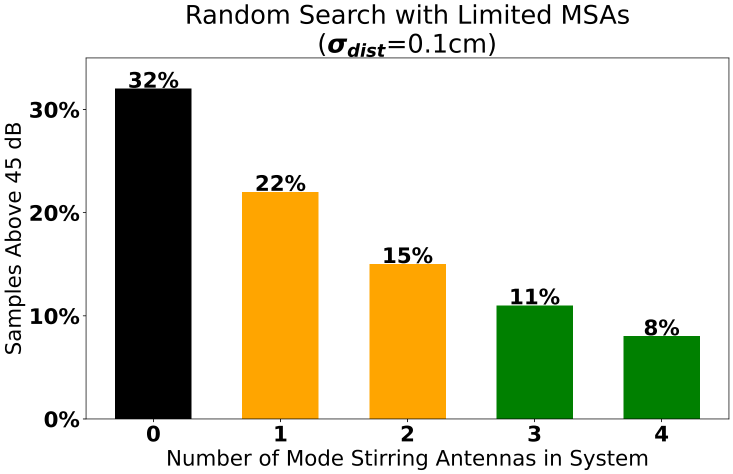

Figure 3.8: Comparison of samples that exceed the threshold for the *Random* reconfiguration strategy as the number of available mode stirring antennas (MSAs) is increased, each simulated with Brownian motion with a σ_{dist} of 0.1 cm per sample.

To understand the benefit of the increased search space of the random search strategy, a secondary simulation was performed. In this case, the same simulation strategy is used, but the search space of states for the random search strategy is limited based on a desired number of MSAs. The zero and four cases are therefore the baseline and random search strategies as previously described, with the one through three cases representing systems with a reduced number of MSAs available. Figure 3.8 displays the percentage of samples exceeding the threshold for these simulations. The benefit of a single antenna is a reduction of roughly 30% of samples exceeding the threshold, reducing the total percentage from 32% in the baseline to 22% for one antenna. Each additional antenna provides a similar relative improvement, though this results in diminishing returns, reaching just 11% and 8% of samples exceeding the threshold for the three and four MSA cases.

3.9 Conclusions

In this chapter, it is shown that an electronic mode stirring system can use a simple random search technique to mitigate path loss in a dynamic system. Though the benefit degrades at high relative motion, a sufficiently high update rate can enable performance improvements to approach the static threshold of improvement. Utilizing a nominal link budget for a BLE backscatter uplink, the system was able to reduce excessive path loss from 32% of samples down to 8% under localized motion scenarios. With only 256 states from 4 MSAs, it was demonstrated that the current electronic mode stirring solution developed presents a *sufficiently stirred* behavior in the 2.4 GHz ISM band, allowing single dominant paths to improve performance. This is improvement is realized even though the stirring contribution itself is generally not over-moded throughout the cage environment.

Chapter 4

Demonstration with BLE Backscatter in the Mode-Stirred Cage Environment

This section is adapted from the author's contributions in the work "Automated Optimization of Electronic Mode Stirring for Enhanced Backscatter Link Margin in Reverberant Cavities," to be submitted in December 2023. This portion of the work utilizes the same integrate electronic mode stirring system [2], but replaces the BCI with a BLE backscatter tag previously described in [4; 25].

4.1 Motivation

To better understand the achieved link margin improvement in an actual backscatter communication system, it is important to measure this effect with an actual backscatter uplink. Having the metal cage environment available and an automated motion system, the only piece required to realize this is a backscatter device and receiver. Fortunately, a Bluetooth Low Energy (BLE) compatible backscatter tag can be used in place of the BCI, serving as the data source [25]. For the receiver an unmodified Android phone is utilized, from which a set of measured received signal strength indicator (RSSI) values can be captured and recorded over the full set of mode stirring states.

4.2 Modified Measurement Setup

The same test fixture as described in Chapter 3 is employed with the following modifications. This BLE backscatter tag replaces the BCI antenna in the cage. It requires an external carrier wave (CW) source set to 2.4145 GHz, which can be provided by the VNA. The VNA will transmit this CW signal at 10 dBm, via the cage-mounted antenna. This allows the tag to repeatedly broadcast an advertising packet at 2.402 GHz – containing the payload "Alice" – to any BLE enabled device. The BLE tag is shown in Figure 4.1b.

(a) **(b)**

Figure 4.1: (a) Google Pixel 6 inside of pet crate with (b) BLE Backscatter tag.

Because the VNA is not capable of receiving the BLE packets, an Android phone will be used instead. A Google Pixel 6 Android phone, in airplane mode, is placed in a corner of the animal crate. Shown in Figure 4.1a, the phone is placed near the wall of the crate so the screen can be seen through the bronze mesh. A free BLE scanning application, running on the Android phone, then reports the received signal strength indicator (RSSI) for each packet, Figure 4.2.

Since the transmit and receive antenna in this system are separated, the link budget is now bi-static. The key difference is that the channel is no longer reciprocal, that is to say the forward and reverse path are different. This means that any inferred one-way path loss measurements are the average of the two separate paths.

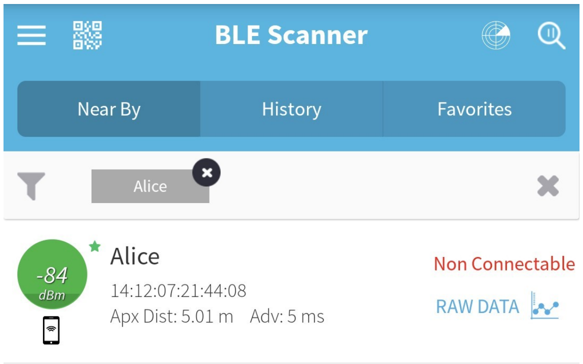

Alice

14:12:07:21:44:08

Apx Dist: 5.01 m Adv: 5 ms

Figure 4.2: BLE Scanner application showing an RSSI measurement from the Android phone.

In this scenario, the motion controller moves the tag to four positions and individual RSSI measurements are manually recorded for every mode stirring state at each position. This is greatly reduced from the sampling of the automated system, due to manual entry of the data.

4.3 Measured Results

Table 4.1: Inferred One-Way Path Loss in Mode Stirring BLE Measurement (Decibels)

(X,Y)	Max (dB)	Mean (dB)	Min (dB)	Range (dB)
(10,10)	34.5	33.1	32.0	2.5
(20,10)	40.0	37.6	35.5	4.5
(30,10)	38.5	36.7	35.0	3.5
(40,10)	42.0	38.8	37.0	5

Table 4.1 indicates the inferred one-way path loss over the stirring states, as computed in equation 4.1. For example, a 40 dB one-way path loss in this case would be equivalent to a -70 dBm RSSI.

$$\text{Inferred One-Way Path Loss dB} = \frac{\text{Transmit Power dBm} - \text{RSSI dBm}}{2} \tag{4.1}$$

The maximum measured one-way path loss was equivalent to a -74 dBm RSSI received signal. No stirring state resulted in the loss of a packet, so all 1024 data points are represented in this data analysis. The dual-polarized electronic mode stirring system has an expected mean improvement of 2.4 dB for one effective MSA and 4.2 dB for two MSAs, see 3.1 in Chapter 3. In these measurements, the improvement ranges are between 2.5-5 dB, with the largest improvement occurring at the position with the greatest one-way path loss. This trend is well aligned with the typical expected behavior of the system and indicated that the largest improvements occur in the highest path loss scenarios.

4.4 Conclusions

This demonstration showed the actual impact on a backscatter uplink when utilizing an electronic mode stirring system. For the four sampled positions, representing positions all within the previously explored link budget, additional margin was gained at all measured locations, with more improvement realized at the more extreme multipath cases. This brief exercise illustrates the effect on BLE compatible uplinks, particularly that the system is capable of generating a *sufficiently stirred* set of multipath states that effect the RSSI received at a receiver.

Chapter 5

Conclusions and Future Work

This thesis presented a thorough analysis of the performance of a 2.4 GHz dual-polarized electronic mode stirring system within a reverberant cavity. This includes the development of an automated reconfiguration system to mitigate multipath for improved link margins. A nominal link budget, based on the Bluetooth Low Energy specification, serves as a starting point for further design of systems in both the biomedical wireless systems that motivated this work as well as other backscatter applications. Through simulation, the system offers a means to mitigate multipath under dynamic motion, with the amount of possible improvement being controlled by the update rate of the configuration. This effect was most prominent in cases of slow-moving scenarios (locally stable), with roughly 10 samples of path similarity before motion begins to severely degrade the system.

A very simple reconfiguration strategy offered improvement over all tested motion behaviors. The strategy utilizes a random search and no knowledge of position information. For slow moving targets, the random search strategy can reduce the number of samples exceeding the threshold by 75% – resulting in only 8% of samples having insufficient link margin, down from the un-stirred 32% of samples. This improved further in the quasi-static cases down to 1% of all samples, meaning that the convergence of the random search is very effective at finding a sufficient state when there are repeated samples at a given position. However, it will be challenging to realize the full benefits of electronic mode stirring in scenarios where the motion velocity outpaces the maximum update rate. In these cases, the percentage begins to exceed 26%, though it still outperforms the no-stirring case. This indicates the importance of the update rate in the system design, as needing to scale with the typical expected velocity for motion.

The system was also shown to be *sufficiently stirred* through the stirring of at least a single dominant mode in 75% of all positions, and was able to satisfy the *well stirred* condition in a minority (40%) of positions. Reaching the *well stirred* criteria in more cases would require more mode stirring antennas or additional phase states, which would increase the search space of possible mode stirring states. The increase in search space could potentially increase the convergence time of the system in real-time operation.

In the final demonstration, the manual measurement of received signal strength for a Bluetooth Low Energy compliant backscatter uplink showed consistent results with the path loss improvements previously observed with the VNA. For the four measured positions, all were distributed near the mean anticipated path loss of the system. The 2-5 dB range of signal strength of the electronic mode stirrer indicates that the system is best suited to remove the worst components of multipath in the environment and does not impact the strong line-of-sight cases.

5.1 Future Work

Further development of the automated reconfiguration system would benefit from integration of the concentrator control into a system sampling in real-time from an active receiver. Having real-time control of the mode stirrer could allow for an experiment with real-world motion and backscatter. This real-world experiment could validate these simulated findings. Furthermore, the inclusion of additional terminations or mode stirring antennas could enable the system to reach the *well stirred* criteria in more positions. The impact on convergence time would be an important metric in relation to the real-time system design. Finally, developing or integrating a localization system within the mode stirring system could allow for the development of improved control algorithms, leveraging a running history of configuration behavior and performance at each position.

Bibliography

[1] A. Oursland, O. Ianchenko, S. M. Reyes, R. Doulgas, M. Lee, and M. S. Reynolds, “Automated Optimization of Electronic Mode Stirring for Enhanced Backscatter Link Margin in Reverberant Cavities,” unpublished, to be submitted Dec. 2023.

[2] S. M. Reyes, A. Oursland, M. Lee, T. J. Moody, and M. S. Reynolds, “Dual-Polarized Electronic Mode Stirring for Improved Backscatter Communication Link Margin in a Reverberant Cavity Animal Cage Environment,” in *2023 IEEE International Conference on RFID (RFID)*, 2023, pp. 25–29.

[3] S. J. Thomas and M. S. Reynolds, “A 96 Mbit/sec, 15.5 pJ/bit 16-QAM modulator for UHF backscatter communication,” in *Proc. IEEE Intl. Conf. RFID (RFID 12)*, Apr. 2012, pp. 185–190.

[4] J. F. Ensworth and M. S. Reynolds, “BLE-Backscatter: Ultralow-power IoT nodes compatible with Bluetooth 4.0 Low Energy (BLE) smartphones and tablets,” *IEEE Trans. Microw. Theory Techn.*, vol. 65, no. 9, pp. 3360–3368, Sept 2017.

[5] E. Voges, T. Eisenburger, and D. Peier, “Electrical mode stirring by reactively loaded antennas in reverberating chambers for EMC,” in *2007 18th Intl. Zurich Symposium Electromagn. Compat.*, 2007, pp. 465–468.

[6] R. Serra, A. C. Marvin, F. Moglie, V. M. Primiani, A. Cozza, L. R. Arnaut, Y. Huang, M. O. Hatfield, M. Klingler, and F. Leferink, “Reverberation chambers a la carte: An overview of the different mode-stirring techniques,” *IEEE Electromagn. Compat. Mag.*, vol. 6, no. 1, pp. 63–78, 2017.

[7] C. T. Moritz, S. I. Perlmutter, and E. E. Fetz, “Direct control of paralysed muscles by cortical neurons,” *Nature*, vol. 456, pp. 639–642, 2008.

[8] A. Jackson, J. Mavoori, and E. E. Fetz, “Correlations between the same motor cortex cells and arm muscles during a trained task, free behavior, and natural sleep in the Macaque monkey,” *Physiology*, vol. 97, no. 1, pp. 360–374, Jan. 2007.

[9] S. Zanos, A. G. Richardson, L. Shupe, F. P. Miles, and E. E. Fetz, “The Neurochip-2: an autonomous head-fixed computer for recording and stimulating in freely behaving monkeys,” *IEEE Trans. Neural Syst. Rehabil. Eng.*, vol. 19, no. 4, pp. 427–435, 2011.

[10] M. Yin *et al.*, “Wireless neurosensor for full-spectrum electrophysiology recordings during free behavior,” *Neuron*, vol. 84, no. 6, pp. 1170 – 1182, 2014.

[11] D. A. Schwarz, M. A. Lebedev, T. L. Hanson, D. F. Dimitrov, G. Lehew, J. Meloy, S. Rajangam, V. Subramanian, P. J. Ifft, Z. Li *et al.*, “Chronic, wireless recordings of large-scale brain activity in freely moving rhesus monkeys,” *Nature Methods*, vol. 11, no. 6, p. 670, 2014.

[12] X. Liu, M. Zhang, A. G. Richardson, T. H. Lucas, and J. V. der Spiegel, “Design of a closed-loop, bidirectional brain machine interface system with energy efficient neural feature extraction and PID control,” *IEEE Trans. Biomed. Circuits Syst.*, vol. 11, no. 4, pp. 729–742, Aug 2017.

[13] R. R. Harrison, H. Fotowat, R. Chan, R. J. Kier, R. Olberg, A. Leonardo, and F. Gabbiani, “Wireless Neural/EMG Telemetry Systems for Small Freely Moving Animals,” *IEEE Trans. Biomed. Circuits Syst.*, vol. 5, no. 2, pp. 103–111, 2011.

[14] J. Rosenthal, A. Sharma, E. Kampianakis, and M. S. Reynolds, “A 25 Mbps, 12.4 pJ/b DQPSK backscatter data uplink for the NeuroDisc brain–computer interface,” *IEEE Trans. Biomed. Circuits Syst.*, vol. 13, no. 5, pp. 858–867, Oct. 2019.

[15] J. Rosenthal and M. S. Reynolds, “A Dual-Band Shared-Hardware 900 MHz 6.25 Mbps DQPSK and 2.4 GHz 1.0 Mbps Bluetooth Low Energy (BLE) Backscatter Uplink for Wireless Brain-Computer Interfaces,” in *2020 IEEE International Conference on RFID (RFID)*, 2020, pp. 1–6.

[16] J. D. Rosenthal, A. Pike, S. Reyes, and M. S. Reynolds, “Electronic Mode Stirring for Improved Backscatter Communication Link Margin in a Reverberant Cavity Animal Cage Environment,” *IEEE Transactions on Antennas and Propagation*, vol. 70, no. 1, pp. 621–630, 2022.

[17] M. Yin, D. Borton, J. Komar, N. Agha, Y. Lu, H. Li, J. Laurens, Y. Lang, Q. Li, C. Bull, L. Larson, D. Rosler, E. Bezard, G. Courtine, and A. Nurmikko, “Wireless neurosensor for full-spectrum electrophysiology recordings during free behavior,” *Neuron*, vol. 84, no. 6, pp. 1170 – 1182, 2014.

[18] M. Ingram, M. Demirkol, and D. Kim, “Transmit diversity and spatial multiplexing for RF links using modulated backscatter,” in *Proc. Intl. Symp. Signals, Syst., and Elect.*, 08 2001, pp. 24–27.

[19] J. D. Griffin and G. D. Durgin, “Gains for RF tags using multiple antennas,” *IEEE Trans. Antennas Propag.*, vol. 56, no. 2, pp. 563–570, 2008.

[20] M. P. Powell, W. R. Britz, J. S. Harper, and D. A. Borton, “An engineered home environment for untethered data telemetry from nonhuman primates,” *J. Neuroscience Methods*, vol. 288, pp. 72 – 81, 2017.

[21] J. Rosenthal, A. Pike, and M. S. Reynolds, “A 1 Mbps 158 pJ/bit Bluetooth Low Energy (BLE) compatible backscatter communication uplink for wireless neural recording in an animal cage environment,” in *Proc. IEEE Intl. Conf. RFID*, 2019, pp. 1–6.

[22] *Bluetooth Core Specification 5.3*, Bluetooth Special Interest Group, Kirkland, WA, USA, July 2021.

[23] G. Andrieu and N. Ticaud, “Performance comparison and critical examination of the most popular stirring techniques in reverberation chambers using the “well-stirred” condition method,” *IEEE Trans. Electromagn. Compat.*, vol. 62, no. 1, pp. 3–15, 2020.

[24] C. Lemoine, P. Besnier, and M. Drissi, “Investigation of Reverberation Chamber Measurements Through High-Power Goodness-of-Fit Tests,” *IEEE Transactions on Electromagnetic Compatibility*, vol. 49, no. 4, pp. 745–755, 2007.

[25] J. F. Ensworth and M. S. Reynolds, “Every smart phone is a backscatter reader: Modulated backscatter compatibility with Bluetooth 4.0 Low Energy (BLE) devices,” in *Proc. 2015 IEEE Intl. Conf. RFID*, 2015.